

## Research Article

# Research on AE Source Location of Linear and Plane Rock Mass

Haiyan Wang,<sup>1,2</sup> Ji Ma ,<sup>2</sup> Gongda Wang ,<sup>3,4</sup> Han Gao,<sup>5</sup> Guangyong Cui,<sup>6</sup> and Xiaoshen Li<sup>7</sup>

<sup>1</sup>China Coal Research Institute, Beijing 100013, China

<sup>2</sup>School of Energy and Mining Engineering, China University of Mining and Technology (Beijing), Beijing 100083, China

<sup>3</sup>State Key Laboratory of the Ministry of Education of China for High-efficient Mining and Safety of Metal Mines, University of Science and Technology Beijing, Beijing 100083, China

<sup>4</sup>School of Civil and Resources Engineering, University of Science and Technology Beijing, Beijing 100083, China

<sup>5</sup>China Coal Energy Research Institute Co., Ltd., Xi'an, Shaanxi 710054, China

<sup>6</sup>Tingnan Coal Industry Co., Ltd., Xianyang, Shanxi 713600, China

<sup>7</sup>Dongpang Coal Mine of Jizhong Energy Group, Zhongxing, Hebei 054000, China

Correspondence should be addressed to Ji Ma; [jm.jewel@outlook.com](mailto:jm.jewel@outlook.com) and Gongda Wang; [wgdcmu@gmail.com](mailto:wgdcmu@gmail.com)

Received 22 May 2020; Revised 6 July 2020; Accepted 29 July 2020; Published 8 September 2020

Academic Editor: Zhen Liu

Copyright © 2020 Haiyan Wang et al. This is an open access article distributed under the Creative Commons Attribution License, which permits unrestricted use, distribution, and reproduction in any medium, provided the original work is properly cited.

The occurrence of rockburst dynamic disaster is a process from the microdamage to macroinstability of coal and rock mass, which is accompanied by the acoustic emission (AE) phenomenon. The application of AE technology can reliably help to judge and predict the damage evolution of coal and rock mass, as the most basic problem in the study of AE is the location of the AE source. In this work, the AE source localization experiments of rod-shaped rocks and plate-shaped rocks were carried out. The influence of calibration wave velocity of linear and plane positioning on the location of the AE source was studied. The feasibility analysis of the AE source localization of a plate-shaped rock with different sensor arrays was conducted. The result of the plane location was optimized by wavelet packet analysis combined with cross correlations. The results show that the homogeneity of marble members in this work is suitable, and the positioning error is least affected by wave velocity. In the positioning of the plane AE source, it is suitable to choose a diamond sensor array. The positioning source should be located near the center of the array network. The positioning effect of the rod-shaped rock is generally better than that of the plate-shaped rock. In the actual source positioning work, it should be simplified as much as possible as a linear positioning problem. A more accurate AE signal delay could be obtained using wavelet packet analysis combined with cross-correlation technology, which can greatly reduce the positioning error caused by the accuracy of time difference. The purpose of this work is to provide a basis for determining a more accurate location of the fracture source of rock materials, which is of great significance and application value on the prediction and control of rockburst dynamic disaster.

## 1. Introduction

In recent years, underground rockburst dynamic disasters have frequently occurred at both home and abroad, resulting in heavy casualties and economic losses [1–5]. In fact, the occurrence of rockburst is the process in which microcracks with continuous staggered initiation between twin and particle interfaces propagate, polymerize, and form into macrocracks, leading to instability and failure. In the entire process, the acoustic emission (AE) phenomenon is present [6, 7]. Nowadays, AE technology is used to monitor the AE signal in the process of coal rock failure and fracture. This

technology can assist in making reliable judgments and predictions on the damaged area, damage degree, and further damage trend of coal and rock, which undoubtedly provides an effective early warning and prevention means to prevent rockburst dynamic disaster [8–10].

A very important part of AE detection is the location of the AE source, that is, the determination of the position of the AE source. A source location point represents an AE event location determined by one or more impacts. The location of the sound source is helpful to evaluate the damage of coal and rock. Jeong and Jang [11–13] analyzed the dispersion characteristics of AE signal in the plate

structure using the wavelet transform method. The time of arrival of the wave to the sensor was obtained, and the AE source was located. Wang and Chu [14] located the friction AE signal of the rotor by wavelet packet analysis combined with the cross-correlation method, obtaining the conclusion that the location accuracy of this method is higher than that of the method directly using the AE signal. Using the theory of modal AE, Jian et al. [15] analyzed the propagation characteristics of elastic waves in metal plates and used the amplitude of wavelet transform to determine the time difference between different waves arriving at the same sensor to locate the linear source of damage. Qi [16] introduced the application of the newly developed signal processing technology based on wavelet transform in the study of crack behavior of composite materials and compared it with the traditional AE technology. The results showed that the analysis results based on wavelet transform are closer to the actual situation than those obtained by the traditional analysis method. Pei et al. [17] studied the spatial evolution and fractal characteristics of natural fractures of marble under uniaxial loading based on AE localization technology. Toyama et al. [18] used the wavelet analysis method to calculate the arrival time of the zero-order spread wave and the zero-order bending wave of the AE signal in the material and realized the accurate location of the AE source. Townsend et al. [19] used an AE monitoring system to locate and track the temporal and spatial evolution of a single discrete compaction zone in the entire diameter range of Diemelstadt sandstone core samples. According to the magnitude frequency distribution of the AE events, the scale of the cracks during the development of the frequency band was described. Naderloo et al. [20] studied the damage progress around joints in brittle materials using AE monitoring technology. In addition, Yang et al. [21], Sedlak et al. [22], Lokajicek et al. [23], and Tang et al. [24] conducted many studies on the location of the AE sources of different materials and the improvement of location accuracy.

It can be seen from the above studies that the original AE signal from the AE source could not be directly monitored up until now, so it is the only effective way to analyze and process the AE signal received by the sensor to obtain the information of the AE source. However, although there are many academic studies on the location of AE sources, the accuracy of the location of AE sources for coal and rock damage is still not very ideal in engineering practice because of the complexity of the internal structure of coal and rock materials. Extracting useful information from the complex AE signals for AE source location and inversion of coal and rock fracture process is still a problem worthy of further study. Moreover, it can be seen from the current research situation that the introduction of wavelet theory into AE signal processing is of great significance for the effective analysis of the AE signal. Based on the arrival time difference positioning theory of the AE signal [25, 26], the accuracy of the obtained wave velocity and arrival time of material is the key factor affecting the positioning accuracy. On the one hand, because the average wave velocity of different areas in the actual rock mass is different, it will inevitably affect the accuracy of the AE source location area, resulting in great

errors. Similarly, the distance between sensors will have a direct effect on the measured value of wave velocity. Therefore, it is necessary to determine the measured wave velocity of material in the sensor array before data acquisition. On the other hand, due to the characteristics of the AE wave, such as the S-wave, P-wave, and surface wave, it will greatly affect the accuracy of the time difference measurement of the sensor.

Therefore, in this work, through the location experiments of the AE sources of the rod-shaped rock and plate-shaped rock, the influence of calibration wave velocity of linear and plane positioning on the location of the AE source was quantitatively studied. The feasibility of the AE source localization of the plate-shaped rock with different sensor arrays was analyzed, and the result of the plane location was optimized by wavelet packet analysis combined with cross correlations. This work provides a basis for determining a more accurate location of the fracture source of underground rock materials, which is of great significance and application value.

## 2. The Wave Velocity Calibration of Samples

*2.1. The Wave Velocity Calibration of Rod-Shaped Rock.* Due to the difference of the wave velocity between different lithology rock materials, G3768 granite (Shandong Wulian Red Granite), GAM marble (Giallo Atlantide Marble), and AAM (Ariston Artificial Marble) artificial stone were selected as the vehicles of acoustic wave in this work.

The location of the simulated acoustic emission source of the wave velocity calibration is the surface of the right end of the rod, and the sensor arrangement in different samples is shown in Table 1.

The positions of the simulated AE sources, the measured directions of the calibrated wave velocities, and the locations of the sensors are shown in Figure 1. The experiment was performed 8 to 10 times in total. Applying formula (1), the wave velocities (P-wave) of different lithological rock materials were obtained and are presented in Table 2:

$$V = \frac{(x_2 - x_1)}{T_2 - T_1}, \quad (1)$$

where  $x_2$  is the position of sensor 2,  $x_1$  is the position of sensor 1, and  $T_2$  and  $T_1$  are the monitoring time of sensor 2 and sensor 1, respectively.

It can be observed from Table 2 that the wave velocity in the same lithology rock material is very close. The calibration results obtained by each group are almost close to the average value. The variation coefficient is a statistic that measures the degree of variation of each observation in the data. Generally, if the variation coefficient of a group of data is greater than 0.15, the group of data is abnormal. The variation coefficients in this experiment are all very small, which fully demonstrates the reliability and authenticity of the experimental scheme. It could be seen that the wave velocity of the artificial rock material is close to that of granite, while the wave velocity of marble is greater than that of granite.

TABLE 1: The coordinates of sensors on the rod-shaped rock samples.

Scientific name	Rock number	Type	Sensor coordinate (cm)	Sensor coordinate (cm)	
			Length $\times$ width $\times$ thickness	$X_1$	$X_2$
Wulian Hong	G3768	Red granite	1440 $\times$ 38 $\times$ 15	23	59
Giallo Atlantide	GAM	Marble	1000 $\times$ 30 $\times$ 18	16	48
Ariston	AAM	Artificial marble	1500 $\times$ 59 $\times$ 12	25	65

Note. The coordinate positions are all relative to the right end of the rod.

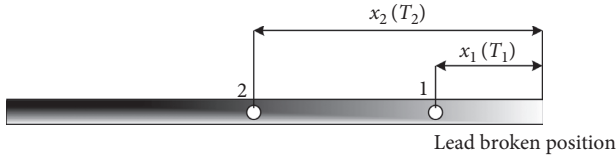


FIGURE 1: The coordinates of AE sources and sensors of rod-shaped rock.

TABLE 2: Results of wave velocity calibration for each group of rod-shaped rock.

Event number	Wave velocity (m/s)		
	G3768	GAM	AAM
1	3157.8947	4304.9520	3200.0000
2	3495.1456	4528.2805	2955.6505
3	3130.4348	4528.3446	3174.6032
4	3354.0477	4485.9394	2863.9550
5	3483.8485	4304.8941	3166.2353
6	3323.0565	4549.7846	3208.5476
7	3506.4821	4549.7199	2970.2897
8	3333.3333	4423.9835	2884.6085
Average value (m/s)	3348.0304	4459.4873	3052.9862
Average error	111.8506	86.1581	134.3603
Variation coefficient	0.0471	0.0249	0.0462

**2.2. The Wave Velocity Calibration of Plate-Shaped Rock.** In this work, two kinds of plate-shaped rocks (G3761-L granite and GAM-L marble) were selected as the vehicles of the acoustic wave. The sensors were set on the surface of the samples in the three directions of  $0^\circ$ ,  $90^\circ$ , and  $45^\circ$  to calibrate the wave velocity, as shown in Figure 2.

In G3761-L, the position of the sensor in the  $0^\circ$  direction was set at the positions of 96 cm and 126 cm, and the pencil lead breakage position was set to 100 cm. The position of sensors was set to 15 cm and 45 cm in the  $90^\circ$  direction, while the pencil lead breakage position was 38 cm. The position of the sensors was set to 10 cm and 52.5 cm in the  $45^\circ$  direction, and the pencil lead breakage position was 15 cm. In GAM-L, the sensors in the  $0^\circ$  direction were set at 72 cm and 105 cm, and the pencil lead breakage position was 96 cm. In the  $90^\circ$  direction, it was 19 cm and 57 cm, respectively, and the pencil lead breakage position was 30 cm. In the  $45^\circ$  direction, it was 5 cm and 55.5 cm, and the pencil lead breakage position was 100 cm. The above positions are distance values relative to the x-y coordinate system in Figure 2. The experiments were performed 4 times for each pencil lead breakage position. According to formula (1), the wave velocities of the samples of different directions in two kinds of plate-shaped rocks are summarized in Table 3.

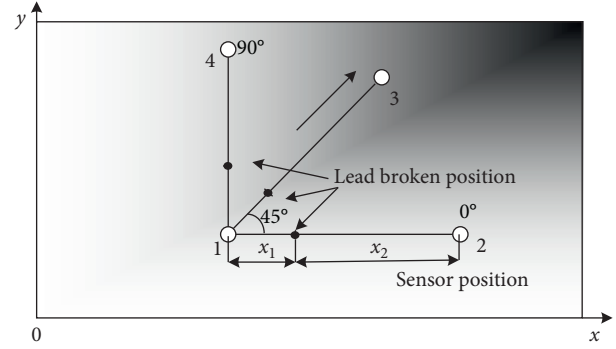


FIGURE 2: The coordinate of AE sources and sensors of plate-shaped rock.

According to the change of the average value, mean error, and variation coefficient related to the wave velocity, it can be seen that the variation coefficient of the calibrated wave velocity of G3761-L in the  $90^\circ$  direction is close to that in the  $45^\circ$  direction. The mean error value in the  $90^\circ$  direction is small. Therefore, it can be concluded that the wave velocity should be about 3380 m/s for G3761-L. The variation coefficient of the calibrated wave velocity of GAM-L in the  $90^\circ$  direction is also close to that of the  $45^\circ$  direction. However, the average error value in the  $45^\circ$  direction is small. Therefore, the calibrated wave velocity of GAM-L should be about 4256 m/s, which is close to the wave velocity of the same lithology rod-shaped rock that was previously calibrated.

### 3. AE Source Positioning Experiment

**3.1. Linear (One-Dimensional) Positioning Experiment.** The AE sensors were arranged at the same two positions on each group of rod-shaped rocks at 5 cm and 100 cm from the right end, respectively, as shown in Figure 3. A pulse-excited source was used as the known source.

The arrival time of three events monitored by sensors on each group of rocks and the known calibrated different wave velocity values were brought into formula (2) to obtain the line positioning results, which was compared with the real coordinate values of three events, as shown in Tables 4–6. Figure 4 was drawn according to the absolute distance error of corresponding positioning results under different event wave velocities.

$$x_s = \frac{1}{2} V \Delta t + \frac{(x_1 + x_2)}{2}, \quad (2)$$

TABLE 3: Results of wave velocity calibration for each group of plate-shaped rock.

Event number	Wave velocity (m/s)					
	G3761-L			GAM-L		
	0°	45°	90°	0°	45°	90°
1	3367.3641	3558.4071	3333.3333	4838.7097	4354.8387	4848.4848
2	3113.1929	3638.0733	3356.6903	4891.2512	4132.6531	4897.9092
3	3113.2369	3624.5218	3404.2553	4832.2796	4268.2927	4705.8824
4	3084.0833	3494.6237	3428.5469	4864.7991	4271.4666	4642.8571
Average value (m/s)	3169.4693	3578.9065	3380.7065	4856.7599	4256.8128	4773.7834
Average error	98.9474	68.5114	35.6947	21.2653	62.0799	99.4136
Variation coefficient	0.0419	0.0185	0.0129	0.0055	0.0216	0.0250

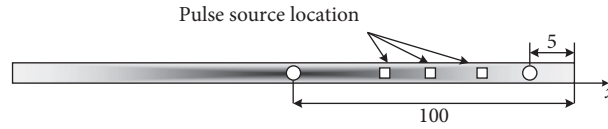


FIGURE 3: The sensor network layout of rod-shaped rock.

TABLE 4: The real coordinates and positioning coordinates of line positioning at different wave velocities in G3768.

Calibration wave velocity (m/s)	Real coordinates and positioning coordinates (cm)					
	Event 1		Event 2		Event 3	
	20	Absolute error	50	Absolute error	70	Absolute error
3157.8947	22.29	2.29	51.55	1.55	67.61	2.39
3495.1456	19.06	0.94	51.45	1.45	69.22	0.78
3130.4348	22.55	2.55	51.56	1.56	67.47	2.53
3354.0477	20.41	0.41	51.49	1.49	68.54	1.46
3483.8485	19.17	0.83	51.45	1.45	69.16	0.84
3323.0565	20.71	0.71	51.50	1.50	68.40	1.60
3506.4821	18.95	1.05	51.45	1.45	69.27	0.73
3333.3333	20.61	0.61	51.50	1.50	68.44	1.56

TABLE 5: The real coordinates and positioning coordinates of line positioning at different wave velocities in GAM.

Calibration wave velocity (m/s)	Real coordinates and positioning coordinates (cm)					
	Event 1		Event 2		Event 3	
	20	Absolute error	50	Absolute error	70	Absolute error
4304.952	20.93	0.93	50.42	0.42	69.65	0.35
4528.2805	19.29	0.71	50.31	0.31	70.54	0.54
4528.3446	19.29	0.71	50.31	0.31	70.54	0.54
4485.9394	19.60	0.40	50.33	0.33	70.37	0.37
4304.8941	20.93	0.93	50.42	0.42	69.65	0.35
4549.7846	19.13	0.87	50.30	0.30	70.62	0.62
4549.7199	19.14	0.86	50.30	0.30	70.62	0.62
4423.9835	20.06	0.06	50.36	0.36	70.12	0.12

TABLE 6: The real coordinates and positioning coordinates of line positioning at different wave velocities in AAM.

Calibration wave velocity (m/s)	Real coordinates and positioning coordinates (cm)					
	Event 1		Event 2		Event 3	
	20	Absolute error	50	Absolute error	70	Absolute error
3200	14.37	5.63	50.69	0.69	68.13	1.87
2955.6505	17.28	2.72	50.83	0.83	66.93	3.07
3174.6032	14.67	5.33	50.70	0.70	68.00	2.00
2863.955	18.37	1.63	50.88	0.88	66.49	3.51
3166.2353	14.77	5.23	50.71	0.71	67.96	2.04
3208.5476	14.26	5.74	50.68	0.68	68.17	1.83
2970.2897	17.10	2.90	50.82	0.82	67.00	3.00
2884.6085	18.13	1.87	50.87	0.87	66.59	3.41

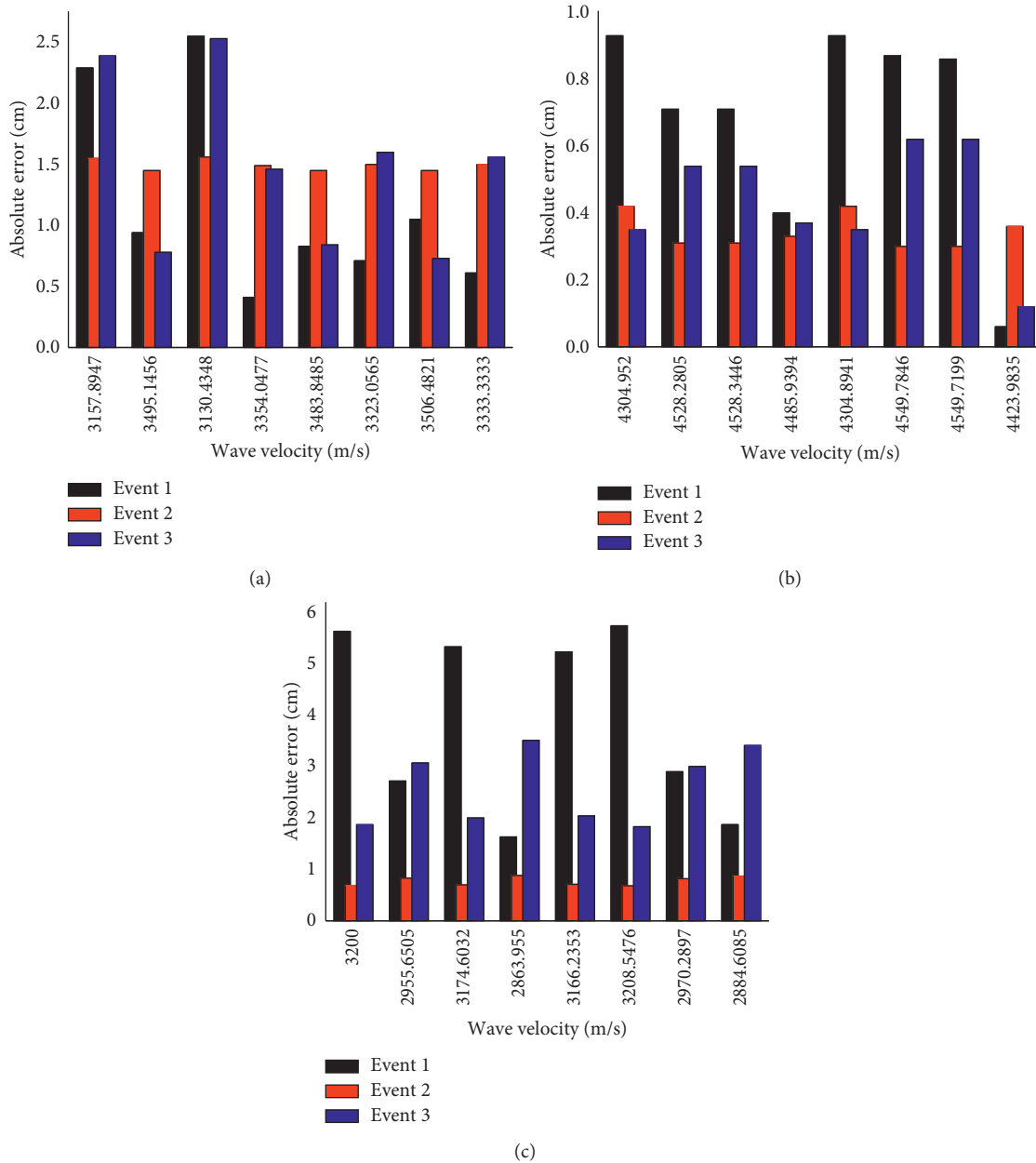


FIGURE 4: The histogram of velocity and absolute error for rod-shaped rock. (a) G376. (b) GAM. (c) AAM.

where  $\Delta t$  is the difference between the arrival times of the acoustic emission signals received by sensors  $x_1$  and  $x_2$ .  $x_s$  represents the linearly located acoustic emission source.

Based on an overall analysis from the perspective of the absolute distance error, it could be seen that different wave velocity settings have a greater impact on the positioning results. When the wave velocities calibrated in G3768 are at 3495.15 m/s and 3483.85 m/s, the absolute distance error is smaller compared with other positioning results in the same group. The absolute errors of Event 1 and Event 3 are stable at about 0.9 cm. Therefore, it can be concluded that the true wave velocity of the granite should be about 3489.5 m/s. When the calibrated wave velocity in the GAM marble is 4448.94 m/s, the absolute error of positioning of each event

is relatively close and small. This value can also be regarded as the quasireal wave velocity of the material. It can also be determined that even the wave velocity changes significantly, as the corresponding absolute distance error is mostly stable below 0.9 cm, indicating that the density and homogeneity of the rock marble material are relatively good. The calibrated wave velocity changes significantly due to the complexity of the composition of the AAM rock. While the real position is at 50 cm, the corresponding absolute errors of the rock materials at different wave velocities are close and small for only Event 2. It is considered that the quasireal wave velocity of this rock material is approximately 2970 m/s. The corresponding absolute errors are 2.9 cm, 0.82 cm, and 3 cm, respectively. According to Figure 5, Event 2 is where the

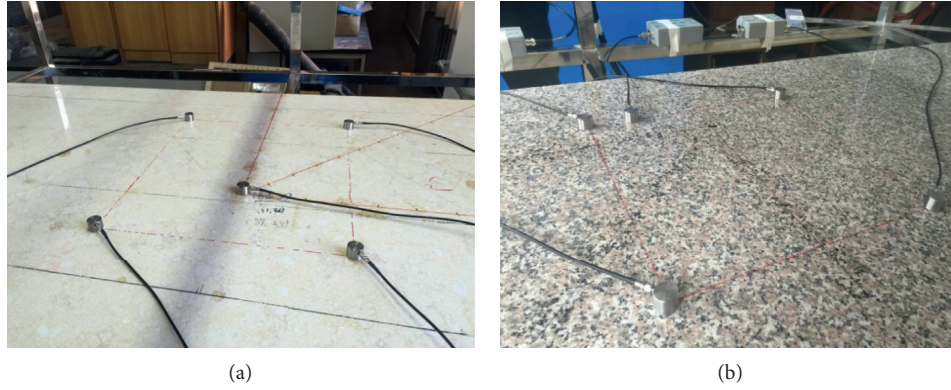


FIGURE 5: The sensor network layout for the plate-shaped rock in Scheme I. (a) GAM-L. (b) G3761-L.

absolute error is relatively close for each group of stones and is selected for analysis. In the G3768, GAM, and AAM, when the difference between the wave velocities is about 220 cm, the corresponding absolute errors are 0.7 cm, 0.11 cm, and 0.13 cm, respectively. All of them are stable at approximately 0.1 cm. To avoid errors caused by the rough application of the average wave velocity for positioning experiments, the above method can be used to find the quasireal wave velocity of the corresponding rock materials. However, due to the heterogeneity of the rock material itself, the absolute error at Event 2 in G3768 is close to 1.5 cm, and the absolute error of Event 1 in AAM is abnormally 5.63 cm when the wave velocity of the material is 3200 m/s. This will have a huge impact on the positioning results. Therefore, the determination of the wave velocity of rock materials still needs more in-depth research.

### 3.2. Plane (Two-Dimensional) Positioning Experiment

**3.2.1. Scheme I of Sensor Layout.** As shown in Figure 5, four sensors were arranged in a rectangular shape on the surfaces of the GAM-L and G3761-L. An additional sensor is used to excite the pulse source with a gain amplifier. The coordinates of each sensor are shown in Table 7. Six source points on the surface of the two plate-shaped rocks were selected. The coordinates of each source point are shown in Table 8. The specific information on the sensors' coordinates and the sources' coordinates are shown in Figure 6.

**3.2.2. Scheme II of Sensor Layout.** As shown in Figure 7, four sensors were arranged in a diamond shape on the surfaces of two plate-shaped rocks. To ensure that the sensors can better receive the AE signals, the sensor and the surface of the rock were coupled with a coupling agent. The pulse excitation source was selected as the known source, and the coordinates of each source point are presented in Table 8. The coordinates of each sensor are exhibited in Table 9. The specific information on the coordinates of each sensor and each source is presented in Figure 8.

TABLE 7: The coordinates of sensors on the plate-shaped rock in Scheme I.

Number	GAM-L		G3761-L	
	X (cm)	Y (cm)	X (cm)	Y (cm)
S1	72	19	96	15
S2	105	19	126	15
S3	105	57	126	45
S4	72	57	96	45

TABLE 8: The coordinates of the pulse sources on the plate-shaped rock.

Focal number	GAM-L		G3761-L	
	X (cm)	Y (cm)	X (cm)	Y (cm)
C1	89	30	111	20
C2	101	44	100	40
C3	80	56(42)	111	30
C4	104	30	124	22
C5	73	20	103	26
C6	90	37	120	39

Note. The C3 focal coordinate of GAM-L in Scheme II is (80, 42).

**3.2.3. Results and Analysis of Focal Location Experiments.** To accurately pick up the first arrival time of each sensor, each source emitted two or three pulse signals. The signals were then played back by DS5 AE analysis software to find the quasireal value of the initial arrival time of each sensor. The first arrival time in the experiment positioning source with two different kinds of sensor layouts in each group of rock is presented in Table 10 to Table 13.

According to the average wave velocity values of the two lithological plate-shaped rocks calibrated in the different directions, MatlabR2012b was used to program and a trust region algorithm (Levenberg–Marquardt algorithm [27]) was used to iteratively solve a series of nonlinear equations composed of formula (3). The positioning results of the selected artificial sources in each group of rocks were obtained, as shown in Tables 14–17. The overall absolute distance error can be obtained according to the positioning errors of the coordinates of the X-coordinate and Y-coordinate, and the absolute distance error histograms of each group of rock at different wave velocities corresponding to the source results are shown in Figure 9.

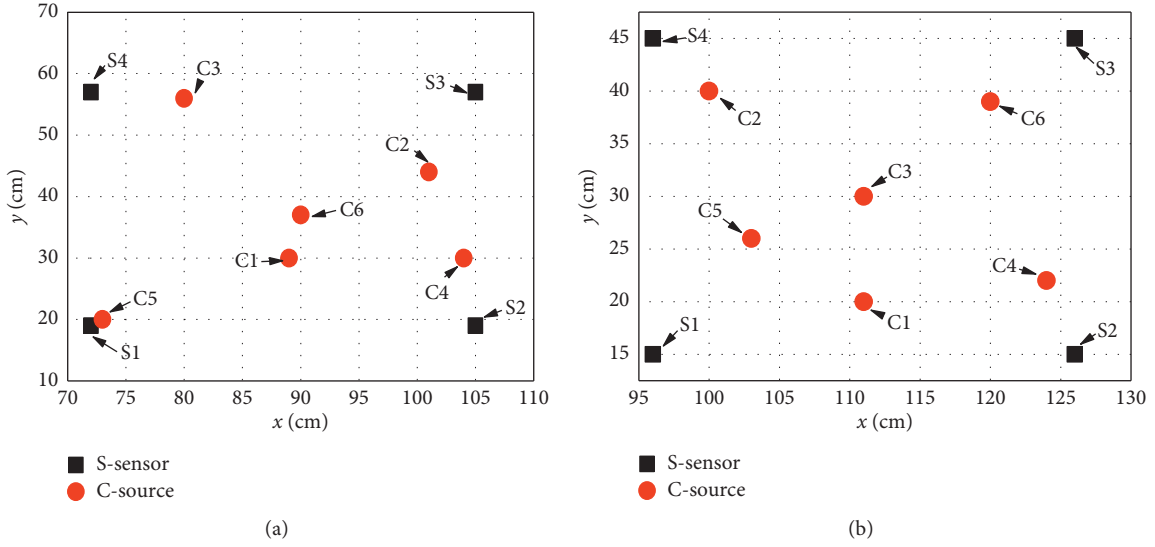


FIGURE 6: The coordinates of pulse sources and sensors in rectangular sensor arrays. (a) GAM-L. (b) G3761-L.



FIGURE 7: The sensor network layout for the plate-shaped rock in Scheme II. (a) GAM-L. (b) G3761-L.

TABLE 9: The coordinates of sensors on the plate-shaped rock in Scheme II.

Sensor number	GAM-L		G3761-L	
	X (cm)	Y (cm)	X (cm)	Y (cm)
S1	88.5	14	111	10
S2	105	38	126	30
S3	88.5	62	111	52
S4	72	38	96	30

$$A_i x_s + B_i y_s = H_i. \quad (3)$$

In formula (3),  $A_i = 2((\alpha_1/d_1) - (\alpha_i/d_i))$ ,  $B_i = 2((\beta_1/d_1) - (\beta_i/d_i))$ , and  $H_i = ((K_1/d_1) - (K_i/d_i))$ . The coordinate of AE source is  $P_s(x_s, y_s)$ , which is unknown. Assuming that  $P_0(x_0, y_0)$  is the sensor closest to the AE source, and additional sensors are arranged at the  $P_i(x_i, y_i)$ . In formula (3),  $d_i = V_i(t_i - t_0)$ , where  $V_i$  is the wave velocity of materials,  $t_i (i = 1, 2, 3)$  is the arrival time of each sensor  $P_i(x_i, y_i)$ ,  $t_0$  is the arrival time of the nearest sensor  $P_0(x_0, y_0)$ .  $K_i = d_i^2 + x_0^2 + y_0^2 - x_i^2 - y_i^2$ ,  $\alpha_i = x_0 - x_i$ , and  $\beta_i = y_0 - y_i$ .

Analyzing the absolute distance errors of plate-shaped rocks GAM-L and G3761-L under different calibrated wave velocities, it could be seen that the wave velocity has a great influence on the positioning results. In experiment Scheme I of GAM-L, when the calibrated wave velocities were 4856.76 m/s and 4773.78 m/s, the absolute distance error value of the C3 source point was abnormally large, and the true coordinate of this point is (80, 56). According to the geometric relationship, the source point is located near the boundary of sensor S3-S4 in the rectangular array, and it is extremely sensitive to the change of wave velocity. It can also be shown in Scheme II that the C5 source point located near the boundary of sensors S1-S4 and the C4 source point located near the boundary of sensors S1-S2 also show the phenomenon that the absolute distance error is unusual. Comparing the absolute distance errors of the two schemes through Figure 9 (GAM-L), the true value of the wave velocity in the marble material is close to 4256.81 m/s, which is consistent with the conclusions obtained in the experiment calibrating the wave velocity of the plate-shaped rock. The overall distance error values calibrated under the wave velocity were compared. The average absolute distance error of the sensors arranged in a rectangular array in Scheme I is 3.6 cm,

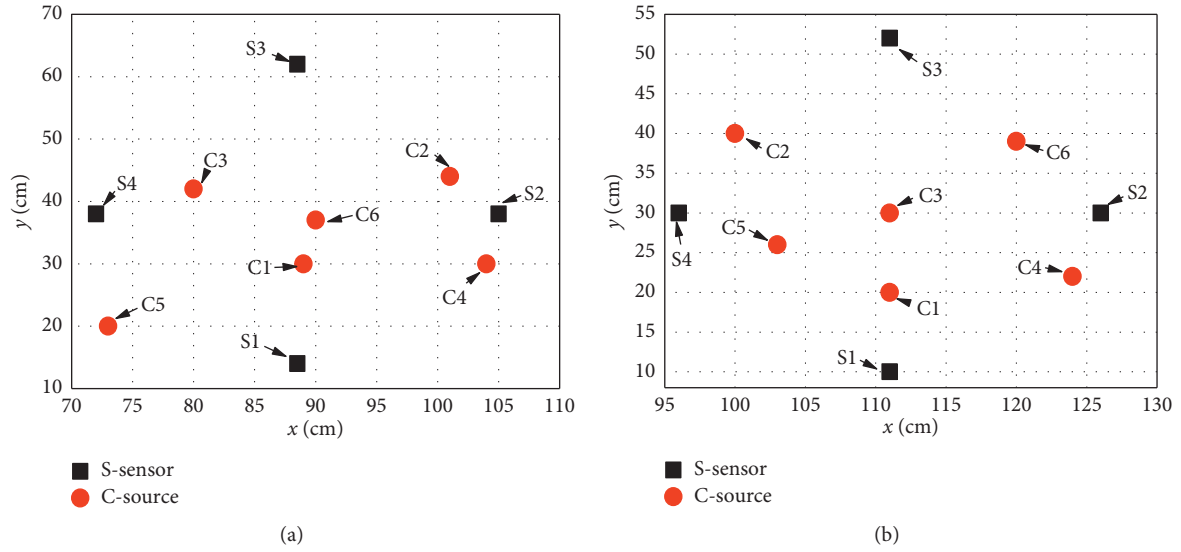


FIGURE 8: The coordinates of pulse sources and sensors in diamond-shaped sensor arrays. (a) GAM-L. (b) G3761-L.

TABLE 10: First arrival time of the pulse sources for Scheme I of GAM-L.

Sensor number	Arrival time (s)					
	C1	C2	C3	C4	C5	C6
S1	1.0667097	21.6454637	42.9266617	63.0944247	79.0673723	93.5269223
S2	1.0667133	21.6454497	42.9266957	63.0943533	79.0674497	93.5269257
S3	1.0667350	21.6454060	42.9266360	63.0944103	79.0674813	93.5269153
S4	1.0667330	21.6454493	42.9265967	63.0944450	79.0674453	93.5269213

TABLE 11: First arrival time of the pulse sources for Scheme I of G3761-L.

Sensor number	Arrival time (s)					
	C1	C2	C3	C4	C5	C6
S1	2.0667040	25.2405140	33.0839133	45.0952613	52.6122573	64.2299640
S2	2.0667063	25.2405550	33.0839210	45.0951953	52.6123047	64.2298807
S3	2.0667320	25.2405260	33.0839167	45.0952373	52.6123027	64.2299000
S4	2.0667367	25.2404637	33.0839160	45.0952703	52.6122780	64.2299460

TABLE 12: First arrival time of the pulse sources for Scheme II of GAM-L.

Sensor number	Arrival time (s)					
	C1	C2	C3	C4	C5	C6
S1	2.1151107	18.0699033	29.4802053	39.5479993	53.5374193	66.6177443
S2	2.1151143	18.0698480	29.4801970	39.5479640	53.5374637	66.6177240
S3	2.1151467	18.0698820	29.4801903	39.5480290	53.5374840	66.6177477
S4	2.1151187	18.0698980	29.4801630	39.5480263	53.5374207	66.6177337

TABLE 13: First arrival time of the pulse sources for Scheme II of G3761-L.

Sensor number	Arrival time (s)					
	C1	C2	C3	C4	C5	C6
S1	2.0666850	22.5086627	44.7673130	62.4902213	80.4045873	97.8702233
S2	2.0667080	22.5086563	44.7672657	62.4901970	80.4046033	97.8701523
S3	2.0667427	22.5086223	44.7673180	62.4902597	80.4046097	97.8701920
S4	2.0667100	22.5086103	44.7673037	62.4902547	80.4045650	97.8702197

TABLE 14: Source location results for Scheme I of GAM-L.

Focal number	Positioning results at different wave velocity levels (cm)											
	4856.7599		Positioning error (cm)		4256.8128		Positioning error (cm)		4773.7834		Positioning error (cm)	
	X	Y	X	Y	X	Y	X	Y	X	Y	X	Y
C1	87.48	30.63	1.52	0.63	87.60	31.57	1.40	1.57	87.50	30.76	1.50	0.76
C2	99.73	47.92	1.27	3.92	98.36	46.69	2.64	2.69	99.54	47.75	1.46	3.75
C3	13.82	146.92	66.18	90.92	79.97	54.22	0.03	1.78	26.16	128.42	53.84	72.42
C4	112.91	22.73	8.91	7.27	108.03	26.11	4.03	3.89	112.14	23.33	8.14	6.67
C5	62.41	17.64	10.59	2.36	67.71	21.60	5.29	1.60	63.48	18.48	9.52	1.52
C6	89.09	39.85	0.91	2.85	89.00	39.62	1.00	2.62	89.07	39.82	0.93	2.82

TABLE 15: Source location results for Scheme I of G3761-L.

Focal number	Positioning results at different wave velocity levels (cm)											
	3169.4693		Positioning error (cm)		3578.9065		Positioning error (cm)		3380.7065		Positioning error (cm)	
	X	Y	X	Y	X	Y	X	Y	X	Y	X	Y
C1	111.26	23.29	0.26	3.29	111.30	22.36	0.30	2.36	111.28	22.81	0.28	2.81
C2	99.15	38.51	0.85	1.49	97.48	39.50	2.52	0.50	98.31	39.02	1.69	0.98
C3	110.06	30.16	0.94	0.15	109.94	30.20	1.06	0.20	110.00	30.16	1.00	0.16
C4	123.03	23.94	0.97	1.94	124.85	23.14	0.85	1.14	123.95	23.53	0.05	1.53
C5	102.61	27.96	0.39	1.96	101.41	27.71	1.59	1.71	102.00	27.83	1.00	1.83
C6	128.46	28.41	8.46	10.59	132.48	28.03	12.5	10.97	130.38	28.23	10.38	10.77

TABLE 16: Source location results for Scheme II of GAM-L.

Focal number	Positioning results at different wave velocity levels (cm)											
	4856.7599		Positioning error (cm)		4256.8128		Positioning error (cm)		4773.7834		Positioning error (cm)	
	X	Y	X	Y	X	Y	X	Y	X	Y	X	Y
C1	89.72	29.37	0.72	0.63	89.53	30.21	0.53	0.21	89.69	29.48	0.69	0.52
C2	102.30	43.90	1.30	0.10	99.90	43.14	1.11	0.87	101.94	43.79	0.94	0.21
C3	79.92	41.85	0.08	0.15	81.16	41.41	1.16	0.59	80.09	41.79	0.09	0.21
C4	111.06	28.77	7.06	1.23	105.67	29.93	1.67	0.07	110.51	28.87	6.51	1.13
C5	67.57	15.44	5.44	4.56	73.92	21.06	0.92	1.06	68.67	16.46	4.33	3.54
C6	90.90	37.19	0.90	0.19	90.56	37.27	0.55	0.27	90.85	37.20	0.85	0.20

TABLE 17: Source location results for Scheme II of G3761-L.

Focal number	Positioning results at different wave velocity levels (cm)											
	3169.4693		Positioning error (cm)		3578.9065		Positioning error (cm)		3380.7065		Positioning error (cm)	
	X	Y	X	Y	X	Y	X	Y	X	Y	X	Y
C1	111.38	20.27	0.38	0.27	111.44	19.64	0.44	0.37	111.41	19.94	0.41	0.06
C2	102.61	38.52	2.61	1.48	100.87	39.62	0.87	0.38	101.75	39.07	1.75	0.93
C3	117.43	30.15	6.43	0.15	118.43	30.04	7.43	0.04	117.94	30.09	6.94	0.09
C4	120.97	23.75	3.03	1.75	123.31	22.49	0.69	0.49	122.08	23.13	1.92	1.13
C5	105.06	27.11	2.06	1.11	104.16	26.59	1.16	0.59	104.60	26.84	1.60	0.84
C6	123.74	36.85	3.74	2.15	126.94	37.73	6.94	1.27	125.29	37.31	5.29	1.69

and that of the sensors arranged in a diamond array is 3.48 cm. Therefore, the diamond-shaped sensor can improve the accuracy of the localization of the source inside the array. Positioning experiments in G3761-L also exhibit abnormal localization points such as C6, C4, and C5. Through a rough comparison, the average absolute distance errors of the rectangular-shaped and diamond-shaped sensor arrays are 4.06 cm

and 3.15 cm, respectively. It also reflects the applicability of the diamond array for 2D AE signal positioning. The wave velocity calibration of G3761-L should be close to 3308.71 m/s.

To analyze the influence degree of positioning accuracy of GAM-L and G3761-L under different sensor arrays and the comparison of the positioning effect under different lithology rocks, the source positioning error and absolute

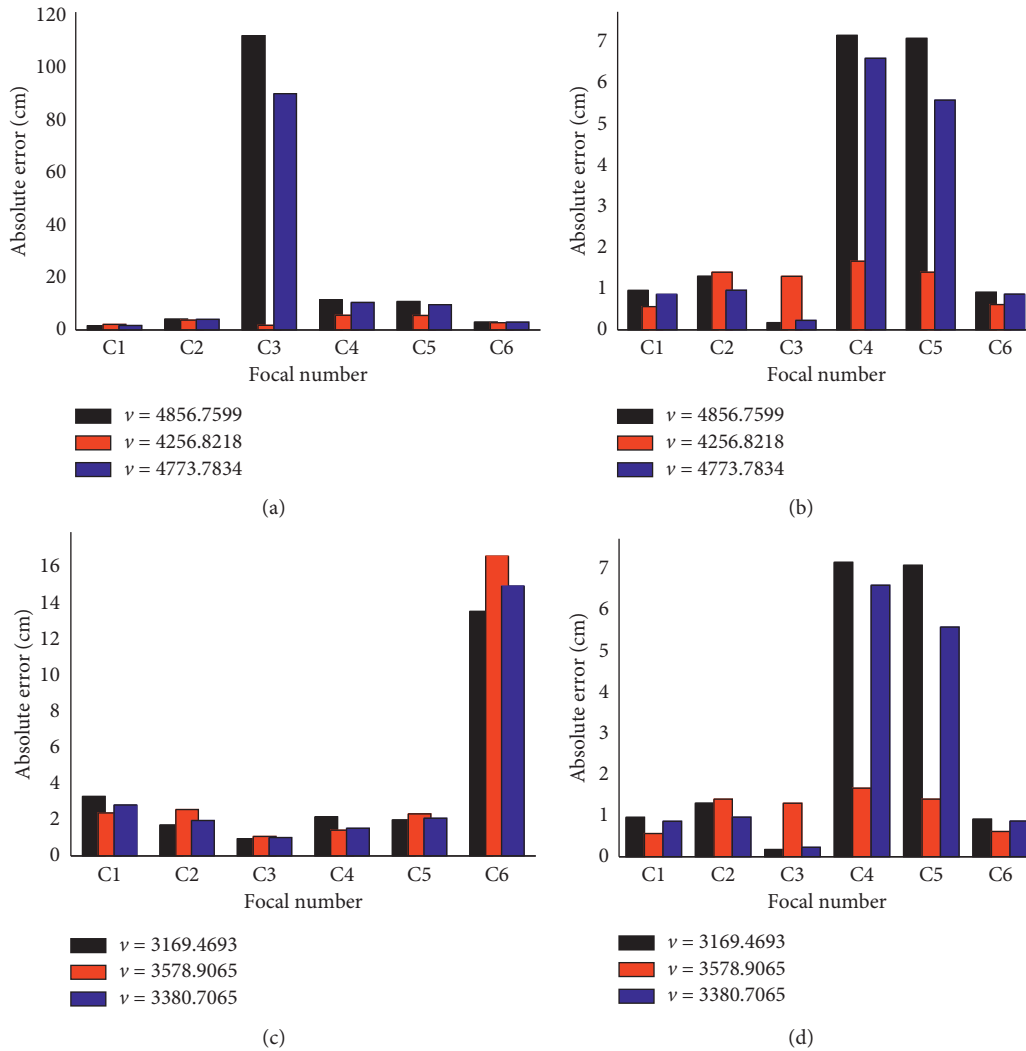


FIGURE 9: Histogram of wave velocity and absolute error of plate-shaped rock. (a) GAM-L in Scheme I, (b) GAM-L in Scheme II, (c) G3761-L in Scheme I, and (d) G3761-L in Scheme II.

distance error under the wave velocity obtained from the above analysis were plotted as a dot chart. The chart is presented in Figure 10.

From Figures 10(a) and 10(b), it can be seen that the positioning error of the rectangular-shaped sensors array is almost more than 1.5 cm, while the positioning error of the diamond-shaped sensors array is less than 1.7 cm, which demonstrates the superiority of the diamond-shaped array for the internal positioning effect. The Y-coordinate error of each point in the diamond-shaped array is less than 1 cm. The X-coordinate error of the source point C1 is 0.53 cm, and its Y-coordinate error is 0.21 cm. The X-coordinate error and Y-coordinate error of source point C6 are 0.55 cm and 0.27 cm, respectively, which is better than other points on positioning accuracy. In terms of their geometric relationship, the true coordinates of C1 and C6 are located near the center of the sensor array. The positioning errors of the X-coordinate, Y-coordinate, and absolute distance in the diamond-shaped sensors array in G3761-L are stable below 2 cm. Among them, the X-coordinates of the C3 and C6

source point are abnormal with an error of more than 5 cm, indicating that the complicated propagation law of the plate wave excited by the pulse source causes an error in the sensor recognition. The errors in the rectangular-shaped array are relatively close, and they are also stable below 2 cm. Except for the abnormal point C6, it is offset from the center of the array and close to the boundary of sensors S2-S3 with a large error of about 11 cm. Comparative analysis shows that the X-coordinate error, Y-coordinate error, and absolute distance error of each source point in the G3761-L granite are below 2 cm and have a good consistency. The variation of different errors of each source point in GAM-L marble is large, indicating that the G3761-L granite plate-shaped rock has better homogeneity within the range of the sensor array, and the authenticity of the receiving arrival time of each sensor is more reliable. The error of each source point obtained by the rectangular-shaped array and the diamond-shaped array in G3761-L is stable below 2 cm. However, by observing the change interval of the X and Y coordinates, it can be found that the change interval of error in the rectangular-shaped

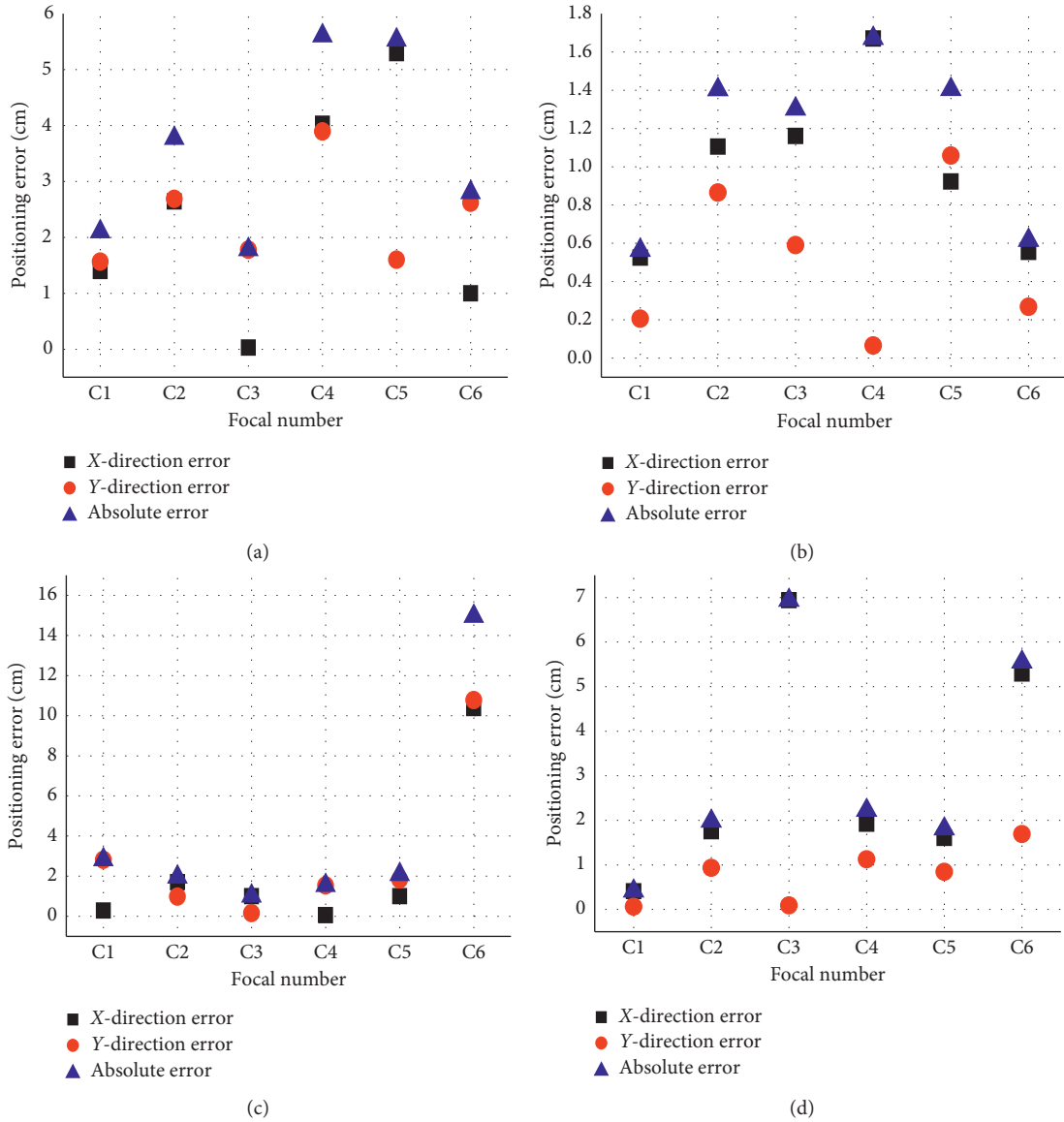


FIGURE 10: The analysis of the location errors of plate-shaped rock. (a) GAM-L in Scheme I, (b) GAM-L in Scheme II, (c) G3761-L in Scheme I, and (d) G3761-L in Scheme II.

array is 0 cm to 4 cm, and that in the diamond-shaped array is 0 cm to 2 cm. Combined with the relevant analysis in the GAM-L, it is concluded that when conducting experimental research on the plane positioning of materials, it is suitable to select a diamond-shaped sensors array and ensure that the monitoring source should be located at the center of the array to avoid the boundary effects.

#### 4. Wavelet Packet Analysis Combined with Cross-Correlation Method to Optimize Source Location

The above discussion is based on experimental conditions and environmental factors. The fixed threshold value to the time difference of the AE source location method was conducted. In fact, the AE signal detected by each AE sensor

is distorted or transformed from the original pulse source. The AE signal can be mixed and superimposed by waves of different forms such as a longitudinal wave, transverse wave, surface wave, and plate wave [28]. In this way, the wave of different modes in the AE signal propagates at different frequencies and velocities, which is bound to cause the dispersion of the signal. If the positioning is carried out simply according to the method of the fixed threshold value, the time difference of the AE signals monitored by each sensor will have a large error. Therefore, the wavelet packet decomposition and reconstruction algorithm of the AE signal waveform analysis method is also introduced, and the signal waveform received by each sensor is processed. Using the cross-correlation method optimizes the traditional fixed threshold pulse source location method.

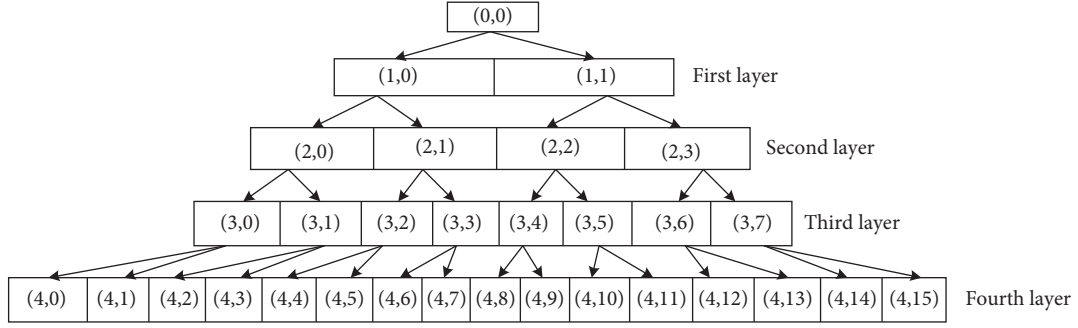


FIGURE 11: The decomposing tree of four-layer wavelet packet.

**4.1. Correlation Analysis of AE Signal.** Correlation in this work represents a linear relationship between variables. For deterministic signals, the relationship between the two variables can be established by functions and corresponded to each other. For such random signals as the AE signals, there is no definite functional relationship between the two random variables. However, there is an approximate relationship that can characterize their characteristics, which is called probability correlation.

For an AE signal  $x(t)$ , its self-correlation function  $R_x(\tau)$  is defined as the average value of the product  $x(t)x(t + \tau)$ :

$$R_x(\tau) = \frac{1}{N} \sum_1^N x(t)x(t + \tau). \quad (4)$$

In the formula,  $x(t + \tau)$  is the new AE signal formed after moving from  $t$  to  $\tau$ .  $\tau$  is the delay time, and the sampling points of the discrete sequence are  $2N$ . The self-correlation function quantitatively describes the degree of similarity between the original waveform and the waveform after a signal is shifted on the time axis [29].

The cross-correlation function of the two AE signals  $x(t)$  and  $y(t)$  is expressed as the average value of the product of signal  $x(t)$  at time  $t$  and  $y(t)$  at time  $t + \tau$ :

$$R_{x,y}(\tau) = \frac{1}{N} \sum_1^N x(t)y(t + \tau). \quad (5)$$

The cross-correlation function can only describe the general dependence between the two signals and cannot represent the degree of correlation between the signals. For this purpose, the correlation number  $\rho_{x,y}$  is introduced:

$$\rho_{x,y} = \frac{R_{x,y}(\tau)}{\sqrt{R_x(0)} \cdot \sqrt{R_y(0)}} \quad |\rho_{x,y}(\tau)| \leq 1. \quad (6)$$

Therefore, before applying the method of the AE source location with the time difference, the time corresponding to the maximum value of the correlation data between the AE signals should be found first, that is, the time difference between the received signals of the two sensors should be determined.

**4.2. Using the Wavelet Packet Analysis with Cross-Correlation Method to Locate the AE Source.** As discussed above, the

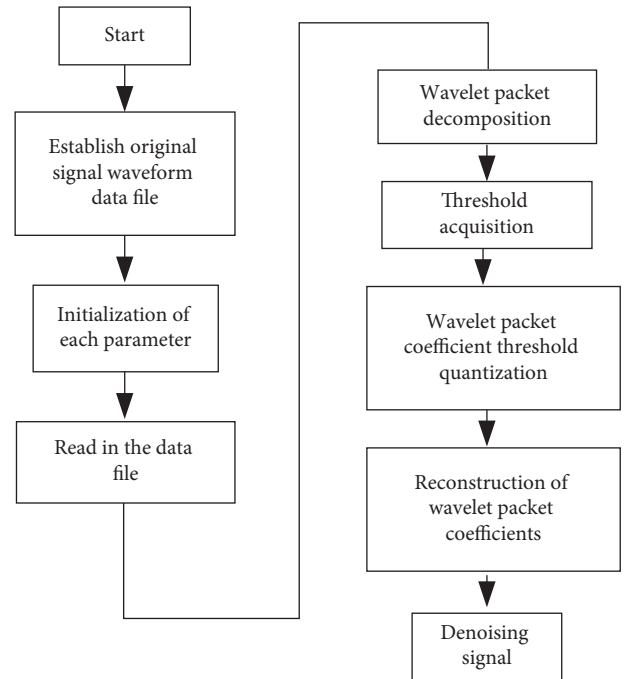


FIGURE 12: The calculating flow diagram.

components of the AE signals generated by pulse excitation are very complex. Therefore, before using the cross-correlation method to find the time difference between two AE signals, the wavelet packet decomposition and reconstruction algorithm should be used to decompose the original AE signal into a frequency band and the wavelet packet coefficient that adapts to the frequency band after decomposition should be extracted. Thus, the arrival time of the elastic wave can be determined more accurately.

The AE source positioning results of the fixed threshold in G3761-L of Scheme II (diamond sensor array) were optimized, and the wave velocity was set to 3380.71 m/s. The DB7 in the wavelet set of the Daubechies series was used as the wavelet basis to decompose the original AE signal [30]. As the frequency distribution of the AE signals of lithologic rock is 0–300 kHz, the number of decomposed layers is usually set as 3–6. In this paper, the number of wavelet packet decomposition layers is set to four, and the specific wavelet packet decomposition tree is shown in Figure 11.

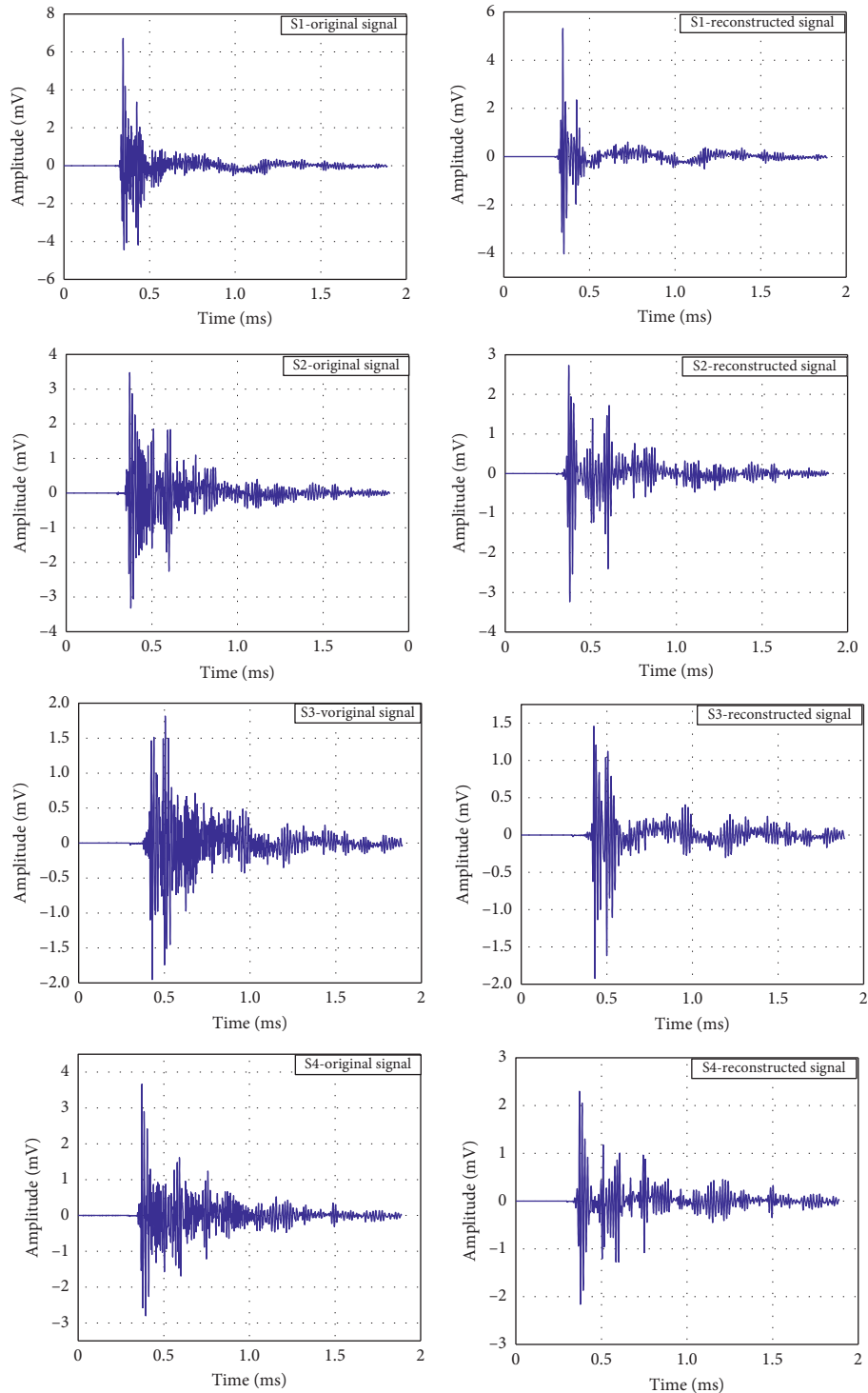


FIGURE 13: Original acoustic emission signal and reconstruction signal from the pulse source C1 received by S1, S2, S3, and S4 sensors.

According to the wavelet packet decomposition coefficient obtained above, the wavelet packet threshold shrinkage method was first applied to denoise the wavelet packet coefficient. Since the reconstructed signal obtained by the soft threshold method is as smooth as the original signal, the wavelet packet coefficient was denoised by the soft threshold. Then, the original signal in each frequency band was

reconstructed according to the wavelet packet coefficient. Since the Nyquist frequency is 1500 kHz, there are 24 wavelet packets. Thus, in the frequency domain, the original signal was decomposed into 16 subbands, each of which was 93.75 kHz wide. MatlabR2012b software was applied to process the algorithm by writing-related programs. Figure 12 presents the flowchart of the algorithm.

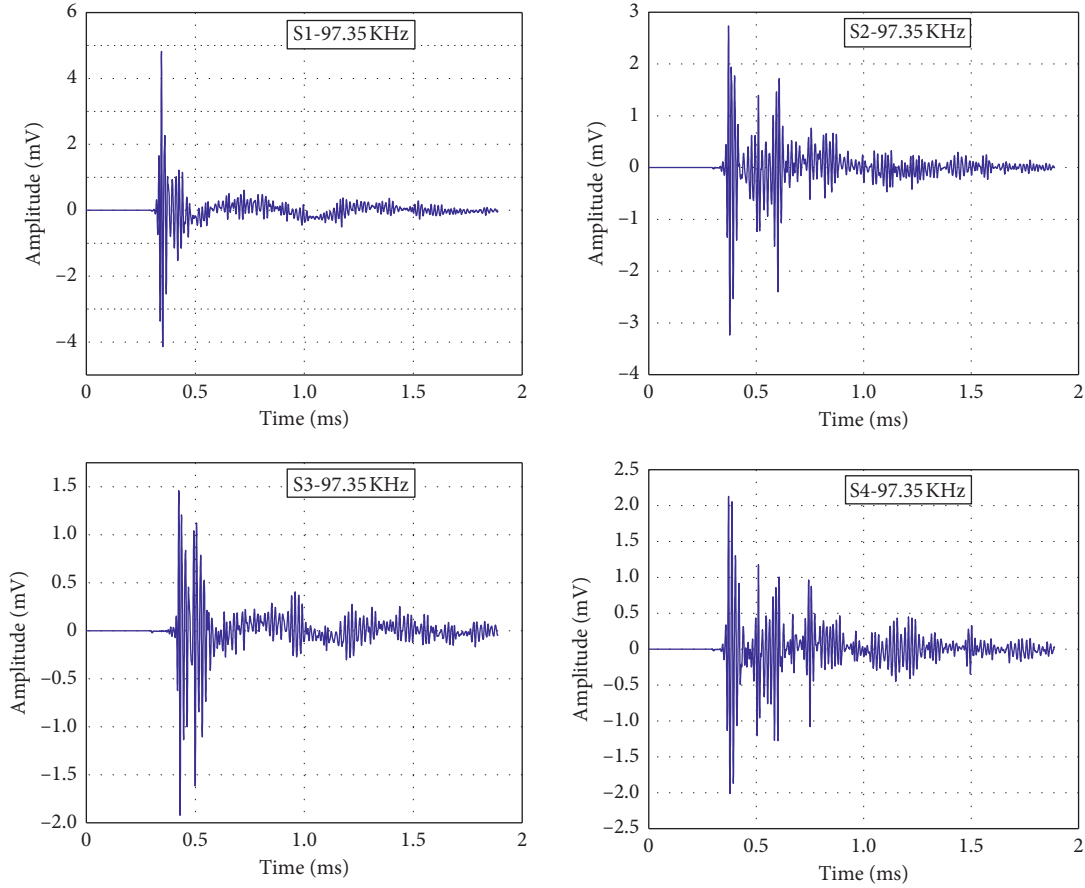


FIGURE 14: Wavelet decomposition waveform at frequency band (4, 0).

Figure 13 shows the original AE signal and reconstruction signal from the pulse source C1 received by the S1, S2, S3, and S4 sensors. Figure 14 shows the decomposition waveform of the original AE signal in the frequency band of 0–97.35 kHz after the reconstruction of the decomposition coefficient of the wavelet packet (4, 0).

As can be seen from Figures 13 and 14, the reconstructed signal of the wavelet packet coefficient obtained by the algorithm after the soft threshold processing is distributed in the frequency band from 0 to 97.35 kHz. The reconstructed signal in the frequency band is very similar to the original reconstructed signal. Therefore, it can truly reflect the original signal and has a single waveform. The reconstructed signals of S1, S2, S3, and S4 within 0–97.35 kHz were correlated with each other to find the time difference between the four AE sensors  $\Delta t_{12}$ ,  $\Delta t_{13}$ ,  $\Delta t_{14}$ ,  $\Delta t_{23}$ ,  $\Delta t_{24}$ , and  $\Delta t_{34}$ . Figure 15 presents the cross-correlation diagram of signals received by each sensor corresponding to the pulse source C1 after wavelet packet decomposition.

According to formulas (4)–(6), the maximum value of the correlation number can be obtained (marked in Figure 15). According to the number of sampling points corresponding to the maximum value, formula (7) can be used to calculate the time difference between the four AE sensors corresponding to the C1–C6 pulse source, as shown in Table 18:

$$\Delta t = \frac{(n - N)}{f}, \quad (7)$$

where  $n$  is the number of sampling points corresponding to the maximum value of the correlation number,  $N$  is the number of sampling points of the original signal, and  $f$  is the sampling frequency set for the experiment.

After determining the time difference between two sensors, the location of the pulse source can be optimized according to the plane time difference location method. Table 19 presents the positioning results of the wavelet packet cross-correlation optimization and the comparison with the original fixed threshold time difference positioning results.

It can be seen from Table 19 that by comparing the time difference location with the fixed threshold, the method in this work achieves a good optimization effect when positioning the time difference. Figure 16 shows the comprehensive comparison of the real pulse source, the experimental location source results, and the wavelet packet decomposition optimization positioning results. It can be clearly seen that the positioning effect after optimization is very significant. The error of the experimental positioning results is large, especially for the three points where the pulsed sources C6, C3, and C4 are close to the edge of the array region. However, their optimized results are very close

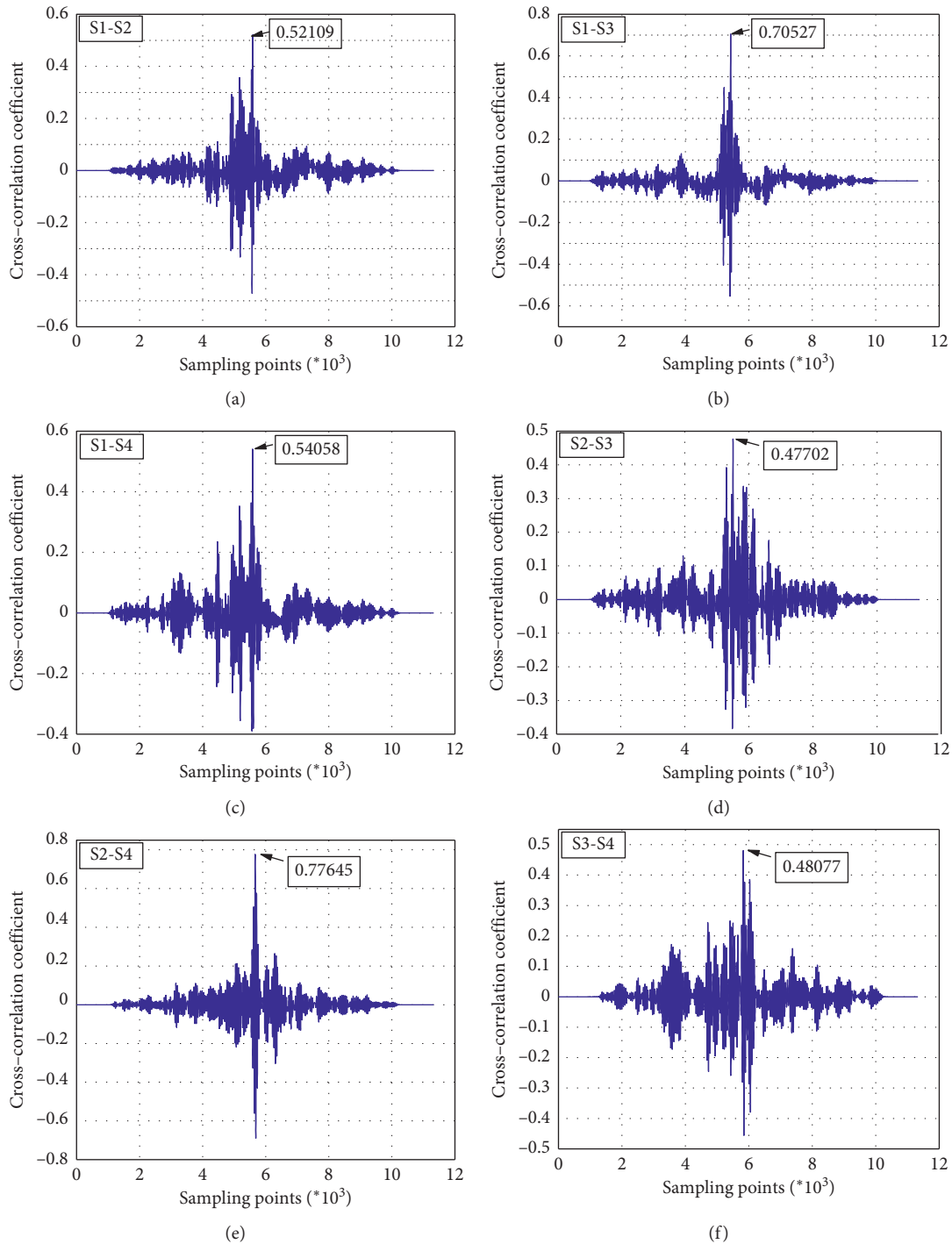


FIGURE 15: Cross-correlation map after wavelet packet decomposition.

to the original source points. Therefore, after the wavelet packet threshold noise is decomposed and reconstructed for the waveform, the cross-correlation analysis is used to obtain the time delay between the sensors receiving the AE signals, and then the time difference is located. This is of certain practical significance. In addition, there are some problems put forward to be further solved. First, the soft threshold is applied to the wavelet packet noise reduction to determine whether the obtained threshold value can be consistent with

the actual signal processing. Second, in the cross-correlation analysis, there is no correlation between the noise in the default random signal and the noise, as well as the noise and sound emission signal. The signal defaults to an infinite continuous sequence. In practice, the signal is often a time-dependent finite sequence, so the traditional cross-correlation analysis will inevitably affect the calculation accuracy of the time difference. Third, the problem of defining the wavelet basis of wavelet packet decomposition also needs to be solved.

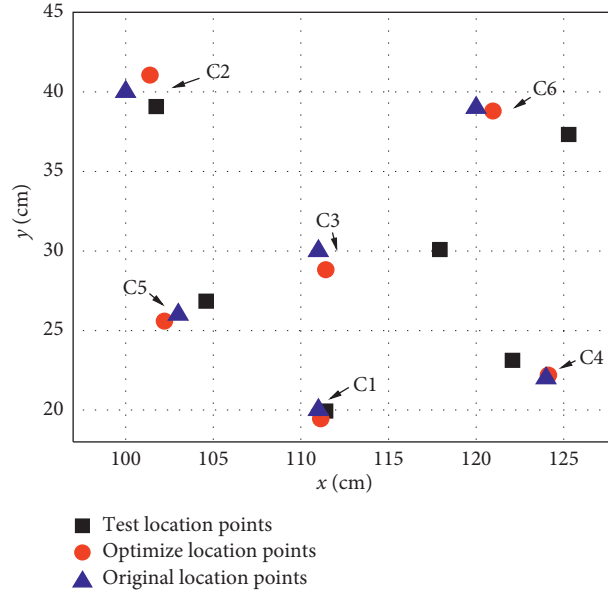


FIGURE 16: The comparison of comprehensive location points.

TABLE 18: Time differences among different sensors determined based on cross-correlation wavelet packet decomposition.

Focal number	Time difference ( $\mu\text{s}$ )					
	$\Delta t_{12}$	$\Delta t_{13}$	$\Delta t_{14}$	$\Delta t_{23}$	$\Delta t_{24}$	$\Delta t_{34}$
C1	-26	-79.7	-26.7	-53	-0.7	52.3
C2	96	44.3	56.3	48.3	60.7	27
C3	22.3	-10	9.3	-32	1	33.3
C4	24.3	-38.3	-33.3	-82.7	-57.7	5.3
C5	-14.3	-31	33.3	-16	47.7	63.7
C6	57.3	33.3	5.7	-11	-50.7	-34.3

TABLE 19: The comparison of positioning results of cross-correlation technique based on wavelet packet decomposition and experiments.

Focal number	Experiment (cm)		Wavelet packet optimization (cm)		Positioning error (cm)	
	X	Y	X	Y	X	Y
C1	111.41	19.94	111.14	19.44	0.138	0.560
C2	101.75	39.07	101.39	41.05	1.390	1.051
C3	117.94	30.09	111.43	28.82	0.430	1.180
C4	122.08	23.13	124.13	22.19	0.130	0.192
C5	104.60	26.84	102.22	25.59	0.780	0.414
C6	125.29	37.31	120.96	38.79	0.960	0.214

## 5. Discussion

In the present work, research has been conducted in three aspects: the influence of wave velocity on the location results of AE sources, the effectiveness analysis of AE source localization in different plane arrays, and the location optimization based on wavelet packet waveform analysis and cross-correlation technology. Although some achievements have been made, it is difficult to regularly grasp the propagation characteristics of elastic waves because of the complexity of elastic waves in real rock masses. Furthermore, AE technology is widely used in the damage detection and defect

location of metal or related materials with good compactness, ductility, and the same nature medium. This technology is lacking strong theoretical support. In addition, there are many uncertain interference factors in the experiment. Therefore, there are still some deficiencies and are areas worthy of improvement. The applicability and accuracy of the AE source location method are closely related to the characteristics of the signal itself, sensor array, and velocity model. Therefore, in practical application, a suitable AE source location method should be adopted according to the characteristics of the specific AE source and propagation medium to minimize the interference caused by an error. In the future, it

is necessary to further explore the AE positioning error caused by the change of specific wave speed and determining how to avoid or minimize such error. Meanwhile, the positioning results could be optimized from the perspective of iterative accuracy of the optimization algorithm.

## 6. Conclusion

- (1) The change of wave velocity-related average value, average error, and the variation coefficient were used to determine the wave velocity of the rock, especially when combining the variation coefficient, which can truly reflect the reliability of the calculated data. The homogeneity of the marble member is better, and the positioning error is least affected by wave velocity.
- (2) For linear positioning, the setting of different wave velocities has an obvious influence on the positioning results. Through the comparison and analysis of the linear positioning results of different wave velocities, the authenticity of the rock wave velocities preliminarily judged by the calibration can be evaluated. The wave velocity of GAM marble is 4485.94 m/s, and the real wave velocity of granite is about 3489.5 m/s.
- (3) In the plane positioning experiment, it is necessary to choose the diamond sensor array to locate the source and ensure that the monitoring source is located in the center of the array network to avoid the influence of boundary effect as much as possible. The positioning effect of the rod-shaped rock is generally better than that of the plate-shaped rock. In the actual source positioning work, it should be simplified as a linear positioning problem as much as possible.
- (4) Through wavelet packet analysis, the original AE signal is denoised by wavelet and decomposed by frequency band. The time difference between sensors is obtained by cross-correlation analysis for the reconstructed signal under a single frequency. The validity of this method is verified by the analysis of experimental data, which proves that this kind of positioning method can effectively improve the positioning accuracy of the source. A reference method is also provided for the research of the real inversion of the AE source.

## Data Availability

The data used to support the findings of this study are available from the corresponding author upon request.

## Conflicts of Interest

The authors certify that they have no conflicts of interest.

## Acknowledgments

This research was funded by the National Natural Science Foundation of China (51804161).

## References

- [1] F. Z. Meng, H. Zhou, Z. Q. Wang et al., "Experimental study on the prediction of rockburst hazards induced by dynamic structural plane shearing in deeply buried hard rock tunnels," *International Journal of Rock Mechanics and Mining Sciences*, vol. 86, pp. 210–223, 2006.
- [2] V. A. Mansurov, "Prediction of rockbursts by analysis of induced seismicity data," *International Journal of Rock Mechanics and Mining Sciences*, vol. 38, no. 6, pp. 893–901, 2001.
- [3] M. C. He, J. L. Miao, and J. L. Feng, "Rock burst process of limestone and its acoustic emission characteristics under true-triaxial unloading conditions," *International Journal of Rock Mechanics and Mining Sciences*, vol. 47, no. 2, pp. 286–298, 2010.
- [4] B. H. G. Brady and E. T. Brown, *Rock Mechanics for Underground Mining*, Allen & Unwin, Crows Nest, Australia, 1985.
- [5] X. Kong, E. Wang, S. Li, H. Lin, Z. Zhang, and Y. Ju, "Dynamic mechanical characteristics and fracture mechanism of gas-bearing coal based on SHPB experiments," *Theoretical and Applied Fracture Mechanics*, vol. 105, Article ID 102395, 2020.
- [6] M. He, F. Ren, and D. Liu, "Rockburst mechanism research and its control," *International Journal of Mining Science and Technology*, vol. 28, no. 5, pp. 829–837, 2018.
- [7] X. Kong, E. Wang, S. Li, H. Lin, P. Xiao, and K. Zhang, "Fractals and chaos characteristics of acoustic emission energy about gas-bearing coal during loaded failure," *Fractals*, vol. 27, no. 05, Article ID 1950072, 2019.
- [8] L. Qiu, D. Song, Z. Li, and J. Liu, "Research on AE and EMR response law of the driving face passing through the fault," *Safety Science*, vol. 117, pp. 184–193, 2019.
- [9] R. P. Liu, D. A. Hutchins, S. Talebi et al., "Laboratory and field investigations of rockburst phenomena using concurrent geotomographic imaging and acoustic emission/microseismic techniques," *Seismicity in Mines*, vol. 129, no. 3-4, pp. 647–659, 1989.
- [10] X. Liu, Z. Liang, Y. Zhang, P. Liang, and B. Tian, "Experimental study on the monitoring of rockburst in tunnels under dry and saturated conditions using AE and infrared monitoring," *Tunnelling and Underground Space Technology*, vol. 82, pp. 517–528, 2018.
- [11] H. Jeong and Y.-S. Jang, "Wavelet analysis of plate wave propagation in composite laminates," *Composite Structures*, vol. 49, no. 4, pp. 443–450, 2000.
- [12] H. Jeong, "Analysis of plate wave propagation in anisotropic laminates using a wavelet transform," *NDT & E International*, vol. 34, no. 3, pp. 185–190, 2001.
- [13] H. Jeong and Y. S. Jang, "Fracture source location in thin plates using the wavelet transform of dispersive waves," *IEEE Transactions on Ultrasonics, Ferroelectrics and Frequency Control*, vol. 47, no. 3, pp. 612–619, 2000.
- [14] Q. Wang and F. Chu, "Experimental determination of the rubbing location by means of acoustic emission and wavelet transform," *Journal of Sound and Vibration*, vol. 248, no. 1, pp. 91–103, 2001.
- [15] J. Jiao, C. He, B. Wu, R. Fei, and X. Wang, "Application of wavelet transform on modal acoustic emission source location in thin plates with one sensor," *International Journal of Pressure Vessels and Piping*, vol. 81, no. 5, pp. 427–431, 2004.
- [16] G. Qi, "Wavelet-based AE characterization of composite materials," *NDT & E International*, vol. 33, no. 3, pp. 133–144, 2000.

- [17] J. Pei, W. Fei, and J. Liu, "Spatial evolution and fractal characteristics of natural fractures in marbles under uniaxial compression loading based on the source location technology of acoustic emission," *Environmental Earth Sciences*, vol. 75, no. 9, p. 828, 2016.
- [18] N. Toyama, J.-H. Koo, R. Oishi, M. Enoki, and T. Kishi, "Two-dimensional AE source location with two sensors in thin CFRP plates," *Journal of Materials Science Letters*, vol. 20, no. 19, pp. 1823–1825, 2001.
- [19] E. Townend, B. D. Thompson, P. M. Benson, P. G. Meredith, P. Baud, and R. P. Young, "Imaging compaction band propagation in Diemelstadt sandstone using acoustic emission locations," *Geophysical Research Letters*, vol. 35, no. 15, pp. 189–193, 2008.
- [20] M. Naderloo, M. Moosavi, and M. Ahmadi, "Using acoustic emission technique to monitor damage progress around joints in brittle materials," *Theoretical and Applied Fracture Mechanics*, vol. 104, Article ID 102368, 2019.
- [21] J. Yang, Y. Wang, H. Gao et al., "Application of wavelet transform to processing the time of acoustic emission waves," *Nondestructive Testing*, vol. 23, no. 11, pp. 482–484, 2001.
- [22] P. Sedlak, Y. Hirose, A. Sabrina et al., "New automatic localization technique of acoustic emission signals in thin metal plates," *Ultrasonics*, vol. 49, pp. 54–262, 2009.
- [23] T. Lokajicek and K. Klima, "A first arrival identification system of acoustic emission signals by means of a high-order statistics approach," *Measurement Science and Technology*, vol. 17, no. 9, pp. 2461–2466, 2006.
- [24] E. L. Tang, Z. Q. Liang, L. Wang, and Y. F. Han, "Experimental investigation on location of debris impact source based on acoustic emission," *Advances in Space Research*, vol. 64, no. 11, pp. 2390–2404, 2019.
- [25] J. Ianniello, "Time delay estimation via cross-correlation in the presence of large estimation errors," *IEEE Transactions on Acoustics, Speech, and Signal Processing*, vol. 30, no. 6, pp. 998–1003, 1982.
- [26] M. G. Amin, "Time-Varying spectrum estimation for a general class of nonstationary processes," *Proceedings of the IEEE*, vol. 74, no. 12, pp. 1800–1802, 1986.
- [27] W. Sun, C. Xu, and D. Zhu, *Optimization Method*, Higher Education Press, Beijing, China, 2010.
- [28] M. Li, Z. Shang, H. Cai, and G. Dong, *Acoustic Emission Detection and Signal Processing*, Science Press, Beijing, China, 2010.
- [29] Y. Kang, *The AE Location Method for Rock-like Materials Based on the Wavelet Analysis*, Northeast University, Boston, MA, USA, 2009.
- [30] Y. Guo, *Research on Wavelet Base Selection for Vibration Signal Processing*, Hefei University of Technology, Hefei, China, 2003.